East European Journal of Physics. 3. 516-525 (2026)
DOI:10.26565/2312-4334-2026-3-47 ISSN 2312-4334

GEOMETRY-INDUCED ELECTRIC FIELD ENHANCEMENT IN PLANAR AND RADIAL Si/GaAs HETEROJUNCTIONS UNDER INCOMPLETE IONIZATION

J.Sh. Abdullayev[1,2], B. Uralov[2], M.Sh. Ibragimova[3]*, B. Tadjibaev[4], M.F. Atayeva[5], G. Boymurodov[6], S.Y. Yusupov[7]

[1]*Institute of Fundamental and Applied Research, National Research University "TIIAME", Tashkent 100000, Uzbekistan*
[2]*National Research University TIIAME, Department of Physics and Chemistry, Tashkent, Uzbekistan*
[3]*Urgench State University, Hamid Olimjon Street, 14, Urgench, 220100, Uzbekistan*
[4]*Tashkent State Technical University, Tashkent, Uzbekistan*
[5]*Bukhara State University, Bukhara 200117, Uzbekistan*
[6]*Navoi State University of Mining and Technologies, Navoi 210100, Uzbekistan*
[7]*Department of Traumatology and Neurosurgery, Bukhara State Medical Institute, Bukhara, Uzbekistan*
**Corresponding Author e-mail: madinabonubahodir2024@gmail.com*
Received April 17, 2026; revised June 28, 2026; in final form August 5, 2026; accepted August 6, 2026

This work presents a comprehensive electrostatic and transport analysis of planar and radial Si/GaAs heterojunctions over the cryogenic-to-room-temperature regime (20–300 K) using self-consistent solutions of the Poisson and carrier continuity equations implemented within advanced semiconductor device simulation frameworks. Particular emphasis is placed on the role of incomplete dopant ionization and its coupling with junction geometry in determining electric-field distribution and carrier transport characteristics. The results demonstrate that incomplete ionization significantly alters the electrostatic behavior of the heterojunctions at cryogenic temperatures, whereas its influence progressively diminishes near room temperature due to enhanced dopant activation. For planar heterojunctions under complete ionization, the maximum electric field decreases from approximately $1.55\cdot10^3$ V/cm at 20 K to $8.5\cdot10^2$ V/cm at 300 K. Incorporation of incomplete ionization reduces the peak field by nearly 50–100 V/cm below 50 K, while producing negligible deviations above 200 K. In contrast, radial heterojunctions exhibit pronounced electric-field localization arising from curvature-induced geometric confinement. Under incomplete ionization, the peak electric field remains within $3.2\cdot10^4$–$3.6\cdot10^4$ V/cm, increasing to $4.2\cdot10^4$–$4.6\cdot10^4$ V/cm for fully activated dopants, corresponding to a geometry-enhanced field amplification of approximately 28–38%. Carrier transport analysis further reveals strong temperature sensitivity of minority carrier injection, which increases by nearly seven orders of magnitude, from 10^2 cm^{-3} at 50 K to 10^9 cm^{-3} at 300 K, whereas majority carrier concentration remains nearly constant at 10^{16} cm^{-3}. The radial architecture additionally produces localized depletion-field enhancement near the cylindrical interface, indicating superior electrostatic confinement compared with conventional planar configurations. These findings establish the coupled influence of geometry, dopant activation, and temperature-dependent transport mechanisms on Si/GaAs heterojunction performance and provide a rigorous framework for the optimization of cryogenic optoelectronic, nanoelectronic, and high-field semiconductor devices.
Keywords: *Si/GaAs heterojunctions; Field distribution; Incomplete dopant ionization; Cryogenic temperatures; Depletion region*

INTRODUCTION

Semiconductor devices constitute the foundation of modern information processing, energy conversion, and photonic technologies [1–3]. Among available material platforms, silicon (Si) has maintained technological dominance due to its scalability, long-term reliability, and compatibility with mature complementary metal–oxide–semiconductor fabrication processes [4–7]. In contrast, gallium arsenide (GaAs) offers distinct advantages, including high electron mobility, a direct bandgap, and strong optical absorption and emission efficiency, making it indispensable for high-speed and optoelectronic applications [8–12]. Owing to these complementary properties, Si and GaAs have become key materials in advanced devices such as radio-frequency transistors, infrared photodetectors, multijunction solar cells, and hybrid optoelectronic systems [13–18].

The integration of Si's cost-effectiveness with GaAs's superior optoelectronic performance has therefore attracted sustained research interest in Si/GaAs heterojunction architectures [19–22]. Recent advances in epitaxial growth, wafer bonding, and interface passivation have significantly improved the structural integrity and electrical stability of Si/GaAs heterostructures [23–27]. Electrical characterization using current–voltage (I–V) and capacitance–voltage (C–V) techniques has further clarified dominant transport mechanisms and junction properties [28–31]. Nevertheless, intrinsic challenges remain. Lattice mismatch, thermal expansion asymmetry, and interface defect states continue to limit device performance, particularly under non-ambient operating conditions [32–35].

These limitations become increasingly severe at low temperatures, where incomplete dopant ionization, carrier freeze-out, and defect-assisted trapping substantially modify electrostatic profiles and transport behavior [36–39]. Reduced ionized dopant density at cryogenic temperatures alters space-charge distributions, suppresses built-in electric fields, and affects breakdown characteristics—issues that are especially critical for space electronics, radiation detectors, and low-noise optoelectronic systems [40–43]. Accurate modeling of such devices therefore requires explicit

Cite as: J.Sh. Abdullayev, B. Uralov, M.Sh. Ibragimova, B. Tadjibaev, M. F. Atayeva,G. Boymurodov, S. Y. Yusupov, East Eur. J. Phys. 3, 516 (2026), https://doi.org/10.26565/2312-4334-2026-3-47

consideration of temperature-dependent dopant activation, which is often neglected in simplified junction analyses [44-46].

To address these challenges, various material and processing strategies—including surface passivation, plasma-assisted bonding, and advanced substrate engineering using liquid-encapsulated Czochralski (LEC), vertical gradient freeze (VGF), and molecular beam epitaxy (MBE)—have been widely explored [47–50]. While these approaches have led to notable improvements in planar Si/GaAs heterojunctions, alternative device geometries remain comparatively underinvestigated. In particular, radial heterojunction configurations offer inherent advantages such as enhanced electric-field localization, increased effective junction area, and improved tolerance to dopant freeze-out effects, yet their electrostatic behavior has not been systematically examined [15,17,32,45].

In this work, a comprehensive comparative analysis of planar and radial Si/GaAs heterojunctions is presented over the temperature range of 20–300 K. The methodology combines analytical solutions of coupled Poisson and carrier continuity equations with calibrated numerical simulations, explicitly incorporating incomplete dopant ionization. By evaluating space-charge density, electrostatic potential, and electric-field distributions, this study elucidates how junction geometry governs low-temperature electrostatics. The results provide quantitative design guidelines for optimizing Si/GaAs heterostructures in cryogenic, radiation-hardened, and high-performance optoelectronic and nanoelectronic applications.

METHODS AND MATERIAL

The Si/GaAs heterojunction was modeled with a p–n junction as the fundamental active element. In the considered structures, boron (B) was adopted as the acceptor dopant for p-type Si, while silicon (Si) was employed as the donor species for n-type GaAs. The parameter set was extracted from established semiconductor databases and experimental reports [26], ensuring consistency with the physical behavior of Si and GaAs. A summary of the parameters employed in the modeling is provided in Table 1.

Table 1. Summary of the electrophysical parameters of Si and GaAs employed in the modeling of the p–n heterostructure in this work at 300 K [45].

Materials	$Eg(eV)$	E_A, $E_D\,(meV)$	$N_C\,(cm^{-3})$	$N_V\,(cm^{-3})$	$n_i\,(cm^{-3})$	g_A, g_D	ε	β_p, β_n
Si	1.12	45	$2.8\cdot10^{19}$	$1.04\cdot10^{19}$	$1.5\cdot10^{10}$	4	11.7	1
GaAs	1.42	5	$4.7\cdot10^{17}$	$7.0\cdot10^{18}$	$1.8\cdot10^{6}$	2	12.9	1

The device simulations incorporated the essential electrophysical parameters of Si and GaAs, including bandgap energy (Eg), donor and acceptor ionization energies (E_D, E_A), effective density of states in the conduction and valence bands (Nc, Nv), intrinsic carrier concentration $n_i(T)$, degeneracy factors of donor and acceptor states (g_D, g_A), relative dielectric constant ε, and electron and hole capture coefficients (βn, βp). All simulations were carried out by solving the coupled Poisson and carrier continuity equations, with explicit treatment of incomplete dopant ionization across the 20–300 K temperature range. Beyond material parameters, device geometry critically influences electrophysical behavior. To enable direct comparison, both planar and radial Si/GaAs heterojunctions were modeled. The adopted dimensions and boundary conditions are summarized in Figure 1, which schematically depicts the investigated structures.

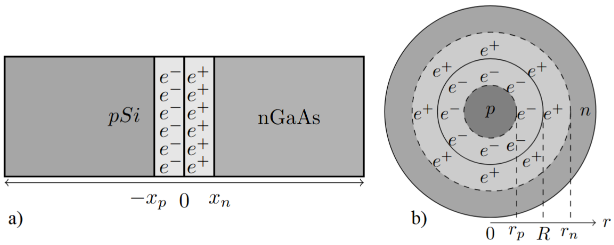

Figure 1. Two-dimensional schematics of the investigated Si/GaAs heterojunctions: (a) planar and (b) radial geometries. The junction comprises p-type Si and n-type GaAs with well-defined depletion regions (x_p, x_n for planar and r_p, r_n for radial configurations). Fixed charges are represented by ionized acceptors *e*− and donors *e*+, while R denotes the core radius in the radial. These structural configurations serve as the foundation for the analytical and numerical modeling of electric field distribution, depletion width, and breakdown behavior across varying doping levels and temperatures.

In the analysis of the electrophysical distributions of the heterojunctions depicted in Figure 1 (a) planar and (b) radial the governing Poisson equation is solved within distinct coordinate frameworks: Cartesian coordinates for the planar configuration and cylindrical coordinates for the radial configuration. In earlier studies [23,24], analytical expressions for planar (Eq. 1) and radial (Eq. 2) heterojunctions have been widely utilized to describe the resulting electrostatic distributions.

Figure 2 shows excellent agreement is achieved between model and experiment, with coefficients of determination R^2 = 0.9860 (Si) and R^2 = 0.9728 (GaAs), confirming deviations remain within 0.01 eV across 180–380 K. For Si, the model predicts a bandgap energy of 1.124 eV at 300 K, in close agreement with the experimental value of 1.122 eV (Δ ≈ 0.002 eV). For GaAs, the calculated bandgap energy is 1.422 eV, compared with the experimental value of 1.424 eV

($\Delta \approx 0.002$ eV). These results validate the calibration of our temperature-dependent model and confirm its reliability for device-level simulations and predictive analyses.

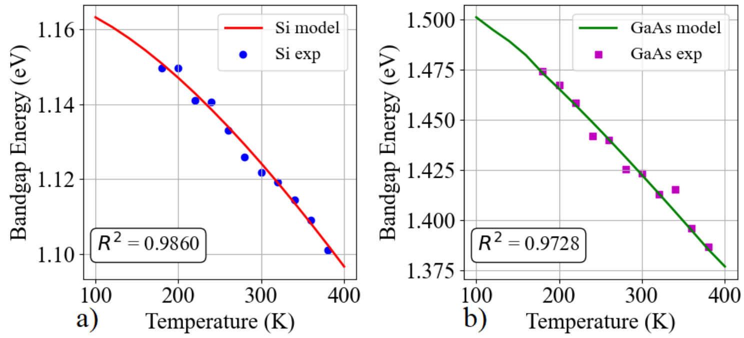

Figure 2. Temperature dependence of the bandgap energy for (a) Si and (b) GaAs, showing comparison between model (solid lines) and experimental data (symbols) [45,46].

$$\frac{d^2\varphi(x)}{dx^2} = \begin{cases} -\dfrac{qN_A}{\varepsilon_{Si}\cdot\varepsilon_0}, & \text{for} \quad -x_p \le x \le 0 \quad (p\text{-Si}) \\ \dfrac{qN_D}{\varepsilon_{GaAs}\cdot\varepsilon_0}, & \text{for} \quad 0 \le x \le x_n \quad (n\text{-GaAs}) \\ 0, & \text{(neutral region)} \end{cases} \tag{1}$$

However, these conventional formulations typically neglect the influence of temperature and applied external bias, factors that can substantially alter the electrostatic behavior of the junction. As a result, their omission may lead to significant inaccuracies when modeling or analyzing devices operating across broad temperature ranges or under both forward and reverse bias conditions.

$$\frac{1}{r}\frac{d}{dr}\left(r\frac{d\varphi(r)}{dr}\right) = \begin{cases} -\dfrac{qN_A}{\varepsilon_{Si}\cdot\varepsilon_0}, & \text{for} \quad r_p \le r \le R \quad (p\text{-Si}) \\ \dfrac{qN_D}{\varepsilon_{GaAs}\cdot\varepsilon_0}, & \text{for} \quad R \le r \le r_n \quad (n\text{-GaAs}) \\ 0, & \text{(neutral region)} \end{cases} \tag{2}$$

In analyzing the electrophysical distributions of heterojunctions (Figure 1), the Poisson equation is solved in Cartesian coordinates for planar and cylindrical coordinates for radial configurations. While conventional formulations (Eqs. 1 and 2) have been widely applied, they often neglect temperature and external bias, leading to inaccuracies across broad operating conditions. Experimental and numerical studies confirm that variations in temperature and applied voltage significantly affect space-charge density, potential, and electric-field profiles. To overcome these limitations, temperature-dependent effects such as self-heating at high temperatures and incomplete ionization at low temperatures were incorporated. The reformulated models introduce additional terms for material parameters, dopant activation energies, carrier distributions, and quantum contributions, yielding new analytical expressions (Eqs. 3 and 4) with improved predictive accuracy.

$$\frac{d^2\varphi(x)}{dx^2} = \begin{cases} -\dfrac{qN_A}{\varepsilon_{Si}\cdot\varepsilon_0\cdot\left(1+\dfrac{g_A\cdot p_p}{\beta_p\cdot N_V(T)}\cdot\exp(\dfrac{\Delta E_A}{kT})\right)}, & \text{for} \quad -x_p \le x \le 0 \quad (p\text{-Si}) \\ \dfrac{qN_D}{\varepsilon_{GaAs}\cdot\varepsilon_0\cdot\left(1+\dfrac{g_D\cdot n_n}{\beta_n\cdot N_C(T)}\cdot\exp(\dfrac{\Delta E_D}{kT})\right)}, & \text{for} \quad 0 \le x \le x_n \quad (n\text{-GaAs}) \\ 0, & \text{(neutral region)} \end{cases} \tag{3}$$

Space-charge density, electrostatic potential, and electric-field distributions were systematically evaluated across a broad temperature range by comparing the conventional formulations (Eqs. 1 and 2) with the newly derived models (Eqs 3 and 4).

$$\frac{1}{r}\frac{d}{dr}\left(r\frac{d\varphi(r)}{dr}\right)=\begin{cases}-\dfrac{qN_A}{\varepsilon_{Si}\cdot\varepsilon_0\cdot\left(1+\dfrac{g_A\cdot p_p}{\beta_p\cdot N_V(T)}\cdot\exp(\dfrac{\Delta E_A}{kT})\right)}, & \text{for } r_p\le r\le R \quad (p\text{-Si})\\ \dfrac{qN_D}{\varepsilon_{GaAs}\cdot\varepsilon_0\cdot\left(1+\dfrac{g_D\cdot n_n}{\beta_n\cdot N_C(T)}\cdot\exp(\dfrac{\Delta E_D}{kT})\right)}, & \text{for } R\le r\le r_n \quad (n\text{-GaAs})\\ 0, & \text{(neutral region)}\end{cases} \tag{4}$$

The graphical analyses reveal pronounced differences in device behavior and demonstrate the superior predictive capability of the revised models. To obtain these solutions, Neumann boundary conditions were imposed by specifying zero electric field at the domain boundaries, $E(r_n)=0$ and $E(r_p)=0$. Dirichlet boundary conditions fixing the electrostatic potential at the contacts were applied in conjunction with appropriate initial conditions, as schematically illustrated in Figure 1 $\varphi(r_p)=0$ $\varphi(r_n)=\varphi_k(T)$. N_D, N_A — total concentration of donors and acceptors, E_f — Fermi level, E_D, E_A — donor and acceptor energy levels, kT — thermal energy.

$$E(x)=\begin{cases}-\dfrac{q\cdot N_A}{\varepsilon_{Si}\cdot\varepsilon_0}\cdot\left(x_p+x\right), & \text{for } -x_p<x<0 \quad \text{(p-Si)}\\ \dfrac{q\cdot N_D}{\varepsilon_{GaAs}\cdot\varepsilon_0}\cdot\left(x_n-x\right), & \text{for } 0<x<x_n \quad \text{(n-GaAs)}\\ 0, & \text{(neutral region)}\end{cases} \tag{5}$$

In the case of the planar p–n junction, expression (5) lacks explicit dependence on both temperature and external bias voltage. This limitation leads to increasing discrepancies in the calculated results, particularly when the model is applied across a broad temperature range.

$$E(r)=\begin{cases}-\dfrac{qN_A}{\varepsilon_{Si}\cdot\varepsilon_0}\cdot\left[r-\dfrac{r_p^2}{r}\right], & \text{for } r_p\le r\le R \quad (p\text{-Si})\\ \dfrac{qN_D}{\varepsilon_{GaAs}\cdot\varepsilon_0}\cdot\left[r-\dfrac{r_n^2}{r}\right], & \text{for } R\le r\le r_n \quad (n\text{-GaAs})\\ 0, & \text{(neutral region)}\end{cases} \tag{6}$$

In the case of the radial p–n junction, expression (6) does not explicitly account for temperature or external bias voltage. Consequently, the model exhibits increasing deviations from the actual electrostatic behavior when applied over broad temperature ranges or under varying bias conditions.

$$E(x,T)=\begin{cases}-\dfrac{q\cdot N_A}{\varepsilon_{Si}\cdot\varepsilon_0\cdot\left(1+\dfrac{g_A\cdot p_p}{\beta_p\cdot N_V(T)}\cdot\exp(\dfrac{\Delta E_A}{kT})\right)}\cdot\left(x_p+x\right), & \text{for } -x_p<x<0 \quad \text{(p-Si)}\\ \dfrac{q\cdot N_D}{\varepsilon_{GaAs}\cdot\varepsilon_0\cdot\left(1+\dfrac{g_D\cdot n_n}{\beta_n\cdot N_C(T)}\cdot\exp(\dfrac{\Delta E_D}{kT})\right)}\cdot\left(x_n-x\right), & \text{for } 0<x<x_n \quad \text{(n-GaAs)}\\ 0, & \text{(neutral region)}\end{cases} \tag{7}$$

The proposed expression (7) for planar p–n junctions incorporates the effects of temperature, dopant activation energy, doping concentration, and material properties, thereby providing a more accurate description of their electrostatic behavior.

The proposed expressions (7) and (8) extend the applicability of analytical models for planar and radial p–n junctions by incorporating temperature dependence, dopant activation energy, doping concentration, and material-specific parameters. Electric field distributions were evaluated under both complete and incomplete ionization, with the latter modeled using Fermi–Dirac statistics. Incomplete ionization reduces the effective space-charge density and lowers the maximum electric field in the depletion region. The results obtained from expressions (5) and (7) for planar junctions and expressions (6) and (8) for radial junctions are presented for Si/GaAs heterojunction structures in the following section.

$$E(r,T)=\begin{cases} -\dfrac{qN_A}{\varepsilon_{Si}\cdot\varepsilon_0\cdot\left(1+\dfrac{g_A\cdot p_p}{\beta_p\cdot N_V(T)}\cdot\exp(\dfrac{\Delta E_A}{kT})\right)}\cdot\left[r-\dfrac{r_p^2}{r}\right], & \text{for } r_p\le r\le R \quad (p\text{-Si}) \\ \dfrac{qN_D}{\varepsilon_{GaAs}\cdot\varepsilon_0\cdot\left(1+\dfrac{g_D\cdot n_n}{\beta_n\cdot N_C(T)}\cdot\exp(\dfrac{\Delta E_D}{kT})\right)}\cdot\left[r-\dfrac{r_n^2}{r}\right], & \text{for } R\le r\le r_n \quad (n\text{-GaAs}) \\ 0, & \text{(neutral region)} \end{cases} \quad (8)$$

RESULTS AND DISCUSSION

This section presents the electrostatic characteristics of planar and radial p–n junctions in Si/GaAs heterostructures. Results obtained from the conventional models (5) and (6) are compared with the proposed formulations (7) and (8) under both complete and incomplete ionization conditions. The analysis highlights their influence on space-charge distribution, electric field profiles, and overall junction behavior across varying operating regimes. The injection characteristics of electrons into the p-side and holes into the n-side of the Si/GaAs heterojunction (Fig. 3) exhibit a strong temperature dependence. At 50 K, minority carrier densities are limited to ~10^2–10^3 cm^{-3} due to incomplete ionization. With increasing temperature, the densities rise progressively: ~ 10^4–10^5 cm^{-3} at 100 K, ~10^6–10^7 cm^{-3} at 200 K, and ~10^8–10^9 cm^{-3} at 300 K.

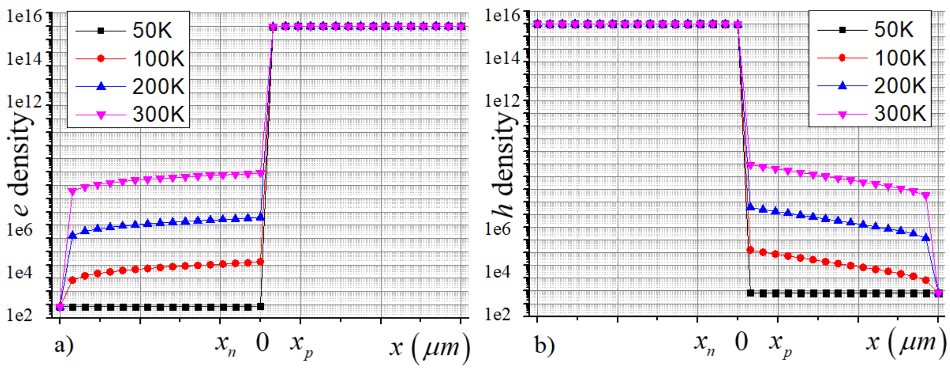

Figure 3. Temperature-dependent injection of (a) electrons into the p-side and (b) holes into the n-side of the Si/GaAs hetero p–n junction. Carrier concentrations are presented for 50 K, 100 K, 200 K, and 300 K.

This nearly seven-order-of-magnitude increase underscores the decisive role of dopant activation in governing injection efficiency. In contrast, majority carrier densities remain fixed at ~10^{16} cm^{-3}, reflecting the imposed doping concentrations. The sharp transition at the metallurgical junction confirms strong electrostatic confinement, while the extended injection profiles reveal the thermal modulation of minority carrier availability. A slight asymmetry is observed, with electrons injected into the p-side (Fig. 3a) exceeding hole injection into the n-side (Fig. 3b), reflecting transport differences across the Si/GaAs interface. Minority carrier injection critically shapes the electrostatic potential and electric field within the depletion region: at low temperatures, dopant freeze-out weakens the built-in field and limits current transport, whereas at higher temperatures, enhanced injection strengthens charge separation but also increases recombination.

Temperature-dependent injection has direct implications for device performance. In solar cells, carrier injection rises from ~10^2 cm^{-3} at 50 K to ~10^9 cm^{-3} at 300 K (a ~7-order increase), strengthening charge separation but also raising recombination at high T. In LEDs and lasers, the observed asymmetry of electrons injected into the p-side reaching up to 10× higher densities than holes in the n-side can reduce radiative efficiency. For photodetectors, injection suppression at low T lowers responsivity by several orders of magnitude, critical for cryogenic or space operation. In high-power/high-frequency devices, variations in space-charge density from ~10^{16} cm^{-3} (majorities) to as low as 10^2 cm^{-3} (minorities at 50 K) significantly alter the built-in potential and field, impacting breakdown and reliability. Injection varying by up to seven orders of magnitude directly links microscopic carrier dynamics with macroscopic device efficiency.

Figure 4 depicts the evolution of the electric-field distribution in planar Si/GaAs heterojunctions as a function of temperature under different ionization assumptions. At 20 K, the maximum electric field reaches approximately

1.55×10^3 V/cm when full dopant activation is assumed, whereas partial ionization limits the peak field to about 1.45×10^3 V/cm. As temperature increases, E_{max} exhibits a monotonic decline in both cases, decreasing to roughly 1.25×10^3 V/cm (complete ionization) and 1.10×10^3 V/cm (incomplete ionization) at 50 K, followed by values near $1.05\times10^3/9.5\times10^2$ V/cm at 100 K, $9.5\times10^2/8.7\times10^2$ V/cm at 200 K, and finally converging to approximately $8.5\times10^2/8.0\times10^2$ V/cm at 300 K. Overall, the reduction in peak field amounts to ~45% for the fully ionized case and ~40% when incomplete ionization is considered.

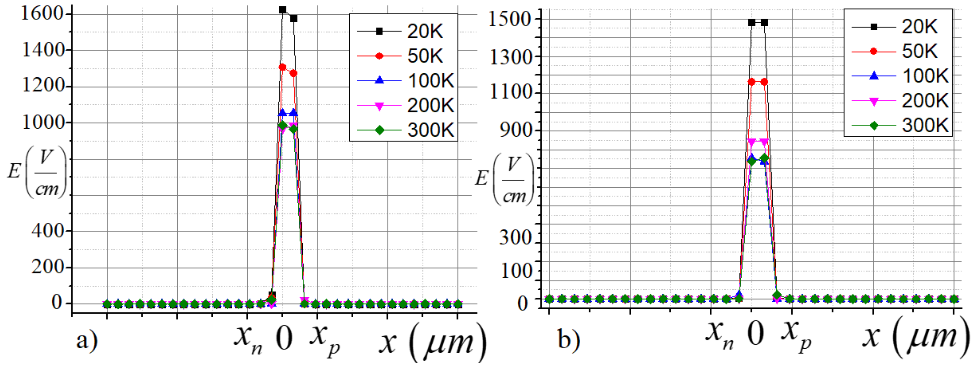

Figure 4. Simulated electric-field profiles for planar Si/GaAs hetero p–n junctions assuming (a) complete dopant ionization and (b) incomplete ionization, evaluated over the temperature range from 20 to 300 K.

The disparity between the two ionization models is most pronounced at cryogenic temperatures, where the difference in E_{max} approaches ~100 V/cm at 20 K due to limited dopant activation. This gap progressively diminishes with increasing temperature and reduces to ~50 V/cm near room temperature, reflecting near-complete ionization of dopants. These trends indicate that incomplete ionization substantially alters junction electrostatics at low temperatures by reducing the built-in potential and suppressing the electric field, while its influence becomes marginal at elevated temperatures. Accurate inclusion of temperature-dependent ionization effects is therefore essential for predictive device modeling and optimization. In cryogenic radiation detectors and space-borne electronics, suppressed electric fields can degrade charge-separation efficiency and timing performance. Similarly, in photovoltaic devices and photodetectors, the temperature-induced reduction of E_{max} directly affects carrier collection efficiency and achievable open-circuit voltage. Incorporating realistic ionization dynamics also improves the reliability of electric-field predictions, aiding in the mitigation of premature breakdown and the optimization of doping profiles. A rigorous understanding of temperature- and ionization-dependent electrostatics thus forms a critical basis for the design of robust, high-efficiency Si/GaAs optoelectronic devices.

Figure 5 illustrates the spatial variation of the radial electric field in Si/GaAs heterojunctions for three different junction radii (R = 0.5, 1.0, and 1.5 µm), highlighting the impact of dopant ionization. In all cases, the electric field reaches its maximum near the depletion boundaries. Under incomplete ionization conditions (case A), peak field values fall within the range of 3.2×10^4–3.6×10^4 V/cm, whereas full dopant activation (case B) increases the peak field to approximately 4.2×10^4–4.6×10^4 V/cm, corresponding to an enhancement of roughly 30–38%. The lower E_{max} observed for incomplete ionization is attributed to the reduced concentration of ionized impurities, which expands the depletion region and consequently weakens the local electric field.

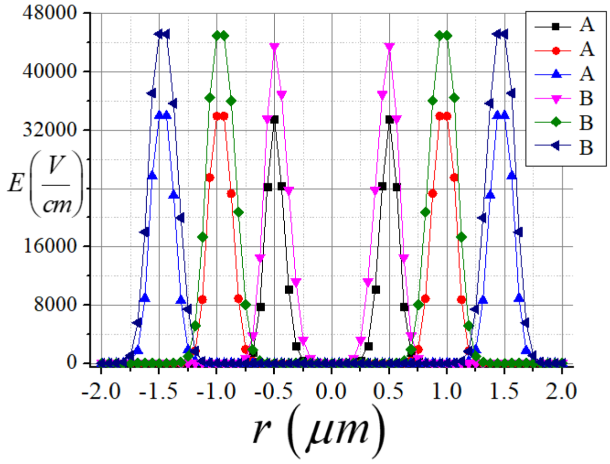

Figure 5. Radial electric field profiles, E(r), calculated for a Si/GaAs hetero p–n junction with cylindrical symmetry. Simulations are shown for device radii of R = 0.5, 1.0, and 1.5 µm. Curves labeled A correspond to partial dopant ionization, whereas curves labeled B represent the fully ionized case.

Table 2. Extracted maximum radial electric field values, E_{max} (V/cm), for Si/GaAs radial p–n junctions under incomplete (A) and complete (B) dopant ionization conditions at different junction radii (R, μm). The relative percentage increase in E_{max} resulting from full dopant activation is also reported.

Radius R (μm)	E_{max} B (V/cm)	E_{max} A (V/cm)	Increase B vs A (%)
0.5	44,000	32,000	37.5
1.0	42,000	32,000	31.3
1.5	46,000	36,000	27.8

In radial architectures, the cylindrical coordinate system intrinsically amplifies the electric field toward the inner radius, whereas the Si/GaAs heterointerface modifies the depletion balance through the contrast in dielectric permittivity between the two semiconductors. As a result, the combined effects of dopant activation, junction radius, and material parameters play a decisive role in shaping the radial electric-field profile. These factors directly impact charge separation efficiency, low-temperature device operation, and susceptibility to high-field phenomena such as premature breakdown in photodetectors and photovoltaic cells. Electric-field maps for planar and radial Si/GaAs hetero p–n junctions under complete and incomplete dopant ionization are shown in Figures 4 and 5.For planar junctions with fully ionized dopants, the maximum electric field E_{max} decreases steadily with temperature, falling from approximately 1.55×10^3 V/cm at 20 K to about 8.5×10^2 V/cm at 300 K. When incomplete ionization is considered, E_{max} is further suppressed by roughly 50–100 V/cm at cryogenic temperatures, reflecting the reduced density of ionized impurities. In contrast, radial heterojunctions develop much stronger electric fields, with peak values of 3.2×10^4–3.6×10^4 V/cm under partial ionization and 4.2×10^4–4.6×10^4 V/cm assuming full activation, corresponding to a relative increase of approximately 28–38%. This enhancement originates from geometric field convergence near the depletion boundary, whereas planar structures distribute the electric field more evenly across the junction region. Across both geometries, partial dopant ionization at low temperatures lowers the effective space-charge concentration, increases the depletion width, and consequently reduces E_{max} These observations emphasize the necessity of incorporating temperature-dependent dopant activation in electrostatic simulations. Overall, radial Si/GaAs heterojunctions enable highly localized electric fields that improve carrier separation and collection, while planar junctions mitigate peak-field stress through more uniform field profiles, highlighting how geometry and ionization physics jointly define device performance.

CONCLUSIONS

In this study, the electrostatic and transport characteristics of planar and radial Si/GaAs heterojunctions were systematically investigated under both complete and incomplete dopant ionization conditions across the temperature range of 20–300 K. By employing self-consistent numerical solutions of the Poisson and carrier continuity equations, the analysis clarifies the coupled effects of junction geometry, dopant activation, and temperature-dependent carrier dynamics on electric-field formation and charge transport. The results reveal that incomplete ionization plays a critical role in determining the low-temperature electrostatic response of the heterojunctions. For planar structures under full dopant activation, the maximum electric field decreases from approximately $1.55 \cdot 10^3$ V/cm at 20 K to $8.5 \cdot 10^2$ V/cm at 300 K. When incomplete ionization is incorporated, the peak field is reduced by approximately 50–100 V/cm at cryogenic temperatures owing to suppressed dopant activation, while the discrepancy becomes negligible above approximately 200 K as thermal ionization approaches completion. Radial heterojunctions exhibit substantially stronger electric-field enhancement than their planar counterparts due to curvature-driven electrostatic confinement. Under incomplete ionization, the maximum electric field remains within $3.2 \cdot 10^4$–$3.6 \cdot 10^4$ V/cm, increasing to $4.2 \cdot 10^4$–$4.6 \cdot 10^4$ V/cm under complete ionization, corresponding to a field amplification of approximately 28–38%. The cylindrical geometry induces pronounced electric-field localization near the depletion boundary, whereas planar heterojunctions maintain comparatively uniform field distributions. Furthermore, a moderate increase in field intensity is observed for smaller junction radii R = 0.5 μm relative to larger radii R = 1.5 μm, consistent with geometric field-focusing effects inherent to radial architectures. The numerical model was further validated through temperature-dependent bandgap calibration against experimental data. Excellent agreement was obtained for both semiconductor materials, with coefficients of determination of R^2 =0.9860 for Si and R^2 =0.9728 for GaAs, while absolute deviations remained below 0.01 eV throughout the 180–380 K interval. At 300 K, the calibrated model predicts bandgap energies of 1.124 eV for Si and 1.422 eV for GaAs, with deviations of approximately 0.002 eV relative to reported experimental values. These results confirm the robustness and physical consistency of the proposed modeling framework. The present study demonstrates that the interplay between incomplete dopant ionization and junction geometry fundamentally governs electric-field distribution, carrier separation efficiency, and transport behavior in Si/GaAs heterostructures. The pronounced electrostatic enhancement observed in radial configurations highlights their potential for next-generation cryogenic optoelectronic, high-field, and nanoscale semiconductor applications. The developed framework further provides a scalable foundation for future investigations involving quantum confinement, interface-state effects, and nonequilibrium transport phenomena in complex heterojunction architectures.

ORCID
Jo'shqin Sh. Abdullayev, https://orcid.org/0000-0001-6110-6616; **M.Sh. Ibragimova,** https://orcid.org/0009-0004-7867-7086
Bakhtiyor Uralov, https://orcid.org/0000-0001-9371-5563;

REFERENCES

[1] Cariou, R., Benick, J., Feldmann, F., Höhn, O., Hauser, H., Beutel, P., and Dimroth, F. "III–V-on-silicon solar cells reaching 33% photoconversion efficiency," Nature Energy, **3**, 326–333 (2018). https://doi.org/10.1038/s41560-018-0131-4

[2] Yao, Z., Yang, G., Han, C., Moya, P. P., Ozkol, E., Yen, J., and Isabella, O. "Poly-SiOx passivating contacts with plasma-assisted N_2O oxidation," Solar RRL, **7**(18), 2300186 (2023). https://doi.org/10.1002/solr.202300186

[3] Mandal, N. C., Biswas, S., Acharya, S., Panda, T., Sadhukhan, S., Sharma, J. R., *et al*., "Properties of SiOx layers for passivation in TOPCon solar cells," Materials Science in Semiconductor Processing, **119**, 105163 (2020). https://doi.org/10.1016/j.mssp.2020.105163

[4] Kang, D., Sio, H. C., Stuckelberger, J., Yan, D., Phang, S. P., Liu, R., and Nguyen, H. T. "Firing stability of p- and n-type polysilicon passivating contacts," Progress in Photovoltaics, **30**(8), 970–980 (2022). https://doi.org/10.1002/pip.3521

[5] Verma, M., Routray, S., Sahoo, G. S., and Mishra, G. P. "Optimization of a-Si thin film solar cell with passivation and c-Si cap layer," Physica Status Solidi (A), **220**(18), 2300213 (2023). https://doi.org/10.1002/pssa.202300213

[6] Saini, A., Srivastava, S.K., Misra, P., and Dutta, M. "Fabrication Techniques of Silicon Microwire Arrays and Realization of Radial Junction Silicon Microwire Solar Cells," in: *Photon to Power. Progress in Optical Science and Photonics*, edited by Ravindran, P., K. G., D., Asok, A., Shankar, D., Ahmed, A.J. (eds) vol 32. (Springer, Singapore, 2025). https://doi.org/10.1007/978-981-96-5914-2_19

[7] Verma, M., and Mishra, G. P. "Electrical analysis of Ta_2O_5 vs SiO_2 tunneling oxides in passivated c-Si cells," International Journal of High Speed Electronics and Systems, **30**(1–2), 2140002 (2022). https://doi.org/10.1142/S0129156421400028

[8] Sahoo, G. S., Harini, C., Mahadevi, N., Nethra, P. S., Tripathy, A., Verma, M., and Mishra, G. P. "CuO film as recombination blocking layer in Si solar cells," Silicon, **15**, 4039–4048 (2023). https://doi.org/10.1007/s12633-023-02701-x

[9] Lepkowski, D. L., Garassman, T. J., Boyer, J. T., Chmielewski, D. J., Yi, C., Juhl, M. K., and Ringel, S. A. "23.4% monolithic epitaxial GaAsP/Si tandem solar cell," Solar Energy Materials and Solar Cells, **230**, 111299 (2021). https://doi.org/10.1016/j.solmat.2021.111299

[10] Li, D., Luo, C., Wang, H., Ling, F., and Yao, J. "Active control of plasmon-induced transparency based on a GaAs/Si heterojunction in the terahertz range," Optical Materials, **114**, 111609 (2021). https://doi.org/10.1016/j.optmat.2021.111609

[11] Hasan, M. N., Zheng, Y., Lai, J., Swinnich, E., Licata, O. G., Baboli, M. A., Mazumder, B., *et al*., "Influences of native oxide on the properties of ultrathin Al_2O_3-interfaced Si/GaAs heterojunctions," Advanced Materials Interfaces, **9**(13), 2101531 (2022). https://doi.org/10.1002/admi.202101531

[12] Jurisch, M., Börner, F., Bünger, T., Eichler, S., Flade, T., Kretzer, U., Köhler, A., Stenzenberger, J., and Weinert, B. "LEC- and VGF-growth of SI GaAs single crystals—Recent developments and current issues," Journal of Crystal Growth, **275**(1–2), 283-291 (2005). https://doi.org/10.1016/j.jcrysgro.2004.10.092

[13] Herfort, J., Schönherr, H.-P., and Ploog, K. H. "Epitaxial growth of hybrid structures," Applied Physics Letters, **83**(18), 3912-3914 (2003). https://doi.org/10.1063/1.1625426

[14] Abdullayev, J. Sh. "Influence of linear doping profiles on the electrophysical features of p-n junctions," East European Journal of Physics, (1), 245–249 (2025). https://doi.org/10.26565/2312-4334-2025-1-26

[15] Heun, S., Sugiyama, M., Maeyama, S., Watanabe, Y., Wada, K., and Oshima, M. "Growth of Si on different GaAs surfaces: A comparative study," Physical Review B, **53**, 13534–13541 (1996). https://doi.org/10.1103/PhysRevB.53.13534

[16] Saxena, P. K., Srivastava, P., and Srivastava, A. "Defect analysis of MBE reactor-grown HgCdTe on Si, GaAs, GaSb, and CZT substrates through the TNL-Epigrow simulator," Journal of Electronic Materials, **53**, 5803–5812 (2024). https://doi.org/10.1007/s11664-024-11082-0

[17] Bardhan Roy, A., Rasulji Valiji, N. H., Mohammad, R., Giridhar, P., and Mondal, P. "Performance enhancement of Si/GaAs based heterojunction solar cells by opto-electronics modeling and optimization," in: *2024 International Conference on Recent Advances in Electrical, Electronics, Ubiquitous Communication, and Computational Intelligence (RAEEUCCI)*, (IEEE, 2024), pp. 1–6. https://doi.org/10.1109/RAEEUCCI61380.2024.10547792

[18] Piriyev, M., Loget, G., Léger, Y., Chen, L., Létoublon, A., Rohel, T., Levallois, C., *et al*., "Dual bandgap operation of a GaAs/Si photoelectrode," Solar Energy Materials and Solar Cells, **251**, 112138 (2023). https://doi.org/10.1016/j.solmat.2022.112138

[19] Jarndal, A., Rakib, F.R. and Alim, M.A. On efficient modeling of drain current for designing high-power GaN HEMT-based circuits. J. Comput. Electron. **23**, 1355–1367 (2024). https://doi.org/10.1007/s10825-024-02225-x

[20] Alanis, J., Gutiérrez-Ojeda, S. J., Méndez-Camacho, R., and Cruz-Hernández, E. "Theoretical investigation of the growth of GaAs on Si(001), Si(110), Si(111), Si(113), and Si(331)," Surfaces and Interfaces, **44**, 103792 (2024). https://doi.org/10.1016/j.surfin.2023.103792

[21] Huang, R., Wang, Q., Guo, Y., and Wang, Z. "Comparative study on GaAs/Si heterojunction fabricated by nitrogen and oxygen plasma activated bonding," Vacuum, **208**, 111735 (2023). https://doi.org/10.1016/j.vacuum.2022.111735

[22] Yamaguchi, M., Takamoto, T., Juso, H., Nakamura, K., Ozaki, R., and Kojima, N. "33.7% efficiency Si tandem solar cell modules," in: *Proceedings of the 2024 IEEE 52nd Photovoltaic Specialist Conference (PVSC)*, (IEEE, 2024). https://doi.org/10.1109/PVSC57443.2024.10749502

[23] Liang, J., Chai, L., Nishida, S., Morimoto, M., and Shigekawa, N. "Investigation on the interface resistance of Si/GaAs heterojunctions fabricated by surface-activated bonding," Japanese Journal of Applied Physics, **54**(3), 030211 (2015). https://doi.org/10.7567/JJAP.54.030211

[24] Haris, M., Loan, S. A., and Mainuddin. "Si/GaAs hetero junction tunnel FET: Design and investigation," Journal of Nanoelectronics and Optoelectronics, **14**(10), 1434–1444 (2019). https://doi.org/10.1166/jno.2019.2575

[25] Liang, J., Miyazaki, T., Morimoto, M., Nishida, S., Watanabe, N., and Shigekawa, N. "Electrical properties of p-Si/n-GaAs heterojunctions by using surface-activated bonding," Applied Physics Express, **6**(2), 021801 (2013). https://doi.org/10.7567/APEX.6.021801

[26] Strzelecka, S., Pawlowska, M., Hruban, A., Gladysz, M., Wegner, E., Gladki, A., and Orlowski, W. "Investigation of As-precipitates in SI GaAs," in: *Solid State Crystals: Growth and Characterization*, edited by J. Zmija, A. Majchrowski, J. Rutkowski, and J. Zielinski, vol. 3178, (SPIE, 1997). pp. 238–241. https://doi.org/10.1117/12.280741
[27] Sapaev, I. B., Razzokov, J. I., Abdullayev, J. S., Qalandarova, D. A., and Ibragimova, M. S. "Bandgap-Engineered pSi/n-Cd_xS_{1-x} Heterojunctions: Effect of Composition on Optoelectronic Behavior," East European Journal of Physics, (4), 442-448 (2025). https://doi.org/10.26565/2312-4334-2025-4-44
[28] Abdullayev, J.S., Qalandarova, D.A., Ibragimova, M.S. *et al*., "Experimental and Simulation-Based Investigation of p-Si/n-CdS Heterojunctions: From Cryogenic Freeze-Out to Room Temperature Operation," J. Electron. Mater. **55**, 2229–2239 (2026). https://doi.org/10.1007/s11664-025-12642-8
[29] Yu, T., Zhang, H., Li, D., and Lu, Y. "Electronic and optical properties of silicene on GaAs(111) with hydrogen intercalation: A first-principles study," RSC Advances, **11**, 16040–16050 (2021). https://doi.org/10.1039/D1RA01959G
[30] Sushkov, A. A., Pavlov, D. A., Andrianov, A. I., Shengurov, V. G., Denisov, S. A., Chalkov, V. Y., Kriukov, R. N., *et al*., "Comparison of III–V heterostructures grown on Ge/Si, Ge/SOI, and GaAs," Semiconductors, **56**, 122–133 (2022). https://doi.org/10.1134/S106378262201012X
[31] Huang, R., Wang, Z., Wu, K., Xu, H., Wang, Q., and Guo, Y. "Hybrid bonding of GaAs and Si wafers at low temperature by Ar plasma activation," Journal of Semiconductors, **45**(4), 042701 (2024). https://doi.org/10.1088/1674-4926/45/4/042701
[32] Seaford, M.L., Tomich, D.H., Eyink, K.G. *et al.*, "Comparison of GaAs grown on standard Si (511) and compliant SOI (511)," J. Electron. Mater. **29**, 906–908 (2000). https://doi.org/10.1007/s11664-000-0179-0
[33] Abdullayev, J.S., Sapaev, I.B., Abdullayev, J.S. *et al.,* "Mathematical Modeling of Incomplete Ionization in Radial *p*-Si/*n*-GaAs Heterojunctions: Temperature and Doping Effects," J. Electron. Mater. **54**, 10484–10492 (2025). https://doi.org/10.1007/s11664-025-12391-8
[34] Baruah, S., Borah, J., Bora, J. *et al.* "Optical modelling of a GaAs/GaSb core–shell cone-topped octagonal-faced nanopillar array with periodic trapezoidal textured cut for high photon trapping efficiency," J. Comput. Electron. **21**, 882–894 (2022). https://doi.org/10.1007/s10825-022-01898-6
[35] Ćalasan, M. Mathematical modeling of solar cells: novel approaches based on Special Trans Function Theory. J. Comput. Electron. **23**, 1137–1147 (2024). https://doi.org/10.1007/s10825-024-02190-5
[36] Ramnarayan, Singh, R., Yadav, P. *et al.* "Numerical modelling of the surface plasmon modes of a circular cylindrical three-layer graphene waveguide," J. Comput. Electron. **24**, 15 (2025). https://doi.org/10.1007/s10825-024-02250-w
[37] Abdullayev J. Sh., Qalandarova D. A., and Ibragimova M. Sh. "Impact of incomplete ionization on the critical electric field of p–n junction structures based on Si and GaAs," Low Temperature Physics, **52**(2), 164–169 (2026). https://doi.org/10.1063/10.0042291
[38] Abdukarimov, A., Rakhmonov, U. S., and Turaev, F. Z. "Dynamic response of the system to external influences," in: *AIP Conference Proceedings* (Vol. 2612, Issue 1, Article 030017). https://doi.org/10.1063/5.0117527
[39] Rakhmonov, U. S., and Matyakubov, Z. K. "Carleman's formula for the matrix domains of Siegel," Chebyshevskii Sbornik, **23**(4), 126–135 (2022). https://doi.org/10.22405/2226-8383-2022-23-4-126-135
[40] Matyakubov, Z. K., Rakhmonov, U. S., Abdullayev, J. S., and Kuromboev, K. "On the Carleman formula for an unbounded matrix domain associated with the classical domain of the second type," Boletim da Sociedade Paranaense de Matematica, **44**(3), 1–8 (2026). https://doi.org/10.5269/bspm.79871
[41] Alanis, J., Gutiérrez-Ojeda, S. J., Méndez-Camacho, R., and Cruz-Hernández, E. (2024). "Theoretical investigation of the growth of GaAs on Si(001), Si(110), Si(111), Si(113) and Si(331)," Surfaces and Interfaces, **44**, 103792. https://doi.org/10.1016/j.surfin.2023.103792
[42] Jahromi, H. D., Zeiri, N., and Lotfiani, A. "CMOS-integrated UV phototransistor utilizing a novel p-GaAs/p-Si staggered heterojunction," Journal of Science: Advanced Materials and Devices, **10**(3), 100891 (2025). https://doi.org/10.1016/j.jsamd.2025.100891
[43] Kumar, T.R., and Priya, G.L. "Temperature and interface trap-induced variations in RF analog and linearity performance of a drain-scaled Si/GaAs uniform tunnel FET dengue nano-biosensor," Microsyst. Technol. **32**, 21 (2026). https://doi.org/10.1007/s00542-025-05976-0
[44] Abdullayev, J. Sh., and Sapaev, I. B. "Experimental and analytical investigation of incomplete ionization in p-Si/n-CdS heterojunctions at cryogenic temperatures," Next Materials, **13**, 102741 (2026). https://doi.org/10.1016/j.nxmate.2026.102741
[45] Geng, P., Li, W., Zhang, X., Zhang, X., Deng, Y., and Kou, H. "A novel theoretical model for the temperature dependence of band gap energy in semiconductors," Journal of Physics D: Applied Physics, **50**(40), 40LT02(2017). https://doi.org/10.1088/1361-6463/aa85ad
[46] Pässler, R. "Semi-empirical descriptions of temperature dependences of band gaps in semiconductors," Physica Status Solidi (b), **236**(3), 710–728 (2003). https://doi.org/10.1002/pssb.200301752
[47] Perera, M. M., Lin, M.-W., Chuang, H.-J., Chamlagain, B. P., Wang, C., Tan, X., Cheng, M. M.-C., *et al*., "Improved Carrier Mobility in Few-Layer MoS2 Field-Effect Transistors with Ionic-Liquid Gating," ACS Nano, **7**(5), 4449–4458 (2013). https://doi.org/10.1021/nn401053g
[48] Musolino, M., Tahraoui, A., Treeck, D. van, Geelhaar, L., and Riechert, H. "A modified Shockley equation taking into account the multi-element nature of light emitting diodes based on nanowire ensembles," Nanotechnology, **27**(27), 275203 (2016). https://doi.org/10.1088/0957-4484/27/27/275203
[49] Han, D.-P., Shin, D.-S., Shim, J.-I., Kamiyama, S., Takeuchi, T., Iwaya, M., and Akasaki, I. "Modified Shockley Equation for GaInN-Based Light-Emitting Diodes: Origin of the Power- Efficiency Degradation Under High Current Injection," IEEE Journal of Quantum Electronics, **55**(4), 1–11 (2019). https://doi.org/10.1109/JQE.2019.2917180
[50] Ali, N. M., Allam, N. K., Abdel Haleem, A. M., and Rafat, N. H. "Analytical modeling of the radial pn junction nanowire solar cells," Journal of Applied Physics, **116**(2), (2014). https://doi.org/10.1063/1.4886596

ГЕОМЕТРИЧНО ЗУМОВЛЕНЕ ПІДСИЛЕННЯ ЕЛЕКТРИЧНОГО ПОЛЯ В ПЛАНАРНИХ І РАДІАЛЬНИХ Si/GaAs ГЕТЕРОПЕРЕХОДАХ ЗА НЕПОВНОЇ ІОНІЗАЦІЇ

Дж.Ш. Абдуллаєв[1,2], Б. Уралов[2], М.Ш. Ібрагімова[3], Б. Таджибаєв[4], М.Ф. Атаєва[5], Г. Боймуродов[6], С.Й. Юсупов[7]
[1]Інститут фундаментальних та прикладних досліджень, Національний дослідницький університет «ТІАМГ», Ташкент 100000, Узбекистан
[2]Національний дослідницький університет ТІАМЕ, кафедра фізики та хімії, Ташкент, Узбекистан
[3]Ургенчський державний університет, вулиця Хаміда Олімджона, 14, Ургенч, 220100, Узбекистан
[4]Ташкентський державний технічний університет, Ташкент, Узбекистан
[5]Бухарський державний університет, Бухара 200117, Узбекистан
[6]Навойський державний гірничо-технологічний університет, Навої 210100, Узбекистан
[7]Кафедра травматології та нейрохірургії, Бухарський державний медичний інститут, Бухара, Узбекистан

Ця робота представляє комплексний електростатичний і транспортний аналіз планарних та радіальних Si/GaAs гетеропереходів у температурному діапазоні від кріогенних до кімнатних температур (20–300 K) із використанням самозгодженого розв’язання рівняння Пуассона та рівнянь неперервності носіїв заряду, реалізованих у сучасних програмних середовищах моделювання напівпровідникових приладів. Особливу увагу приділено ролі неповної іонізації домішок та її взаємозв’язку з геометрією переходу у формуванні розподілу електричного поля та транспортних характеристик носіїв заряду. Отримані результати демонструють, що неповна іонізація суттєво впливає на електростатичну поведінку гетеропереходів за кріогенних температур, тоді як її вплив поступово зменшується поблизу кімнатної температури внаслідок посилення активації домішок. Для планарних гетеропереходів за умови повної іонізації максимальне електричне поле зменшується приблизно від 1.55×10^3 В/см при 20 K до 8.5×10^2 В/см при 300 K. Урахування неповної іонізації призводить до зниження пікового поля приблизно на 50–100 В/см нижче 50 K, тоді як вище 200 K відхилення стають практично незначними. На відміну від цього, радіальні гетеропереходи характеризуються вираженою локалізацією електричного поля, зумовленою геометричним обмеженням, пов’язаним із кривизною структури. За умов неповної іонізації пікове електричне поле перебуває в межах 3.2×10^4–3.6×10^4 В/см, збільшуючись до 4.2×10^4–4.6×10^4 В/см у випадку повністю активованих домішок, що відповідає геометрично зумовленому підсиленню поля приблизно на 28–38%. Аналіз транспорту носіїв також виявив високу температурну чутливість інжекції неосновних носіїв, концентрація яких зростає майже на 7 порядків — від $\sim1\times10^2$ см$^{-3}$ при 50 K до $\sim1\times10^9$ см$^{-3}$ при 300 K, тоді як концентрація основних носіїв залишається майже сталою на рівні $\sim1\times10^{16}$ см$^{-3}$. Радіальна архітектура додатково забезпечує локалізоване підсилення поля в області збіднення поблизу циліндричного інтерфейсу, що свідчить про ефективніше електростатичне обмеження порівняно з традиційними планарними конфігураціями. Отримані результати встановлюють комплексний взаємозв’язок між геометрією структури, активацією домішок та температурно-залежними механізмами транспорту під час формування характеристик Si/GaAs гетеропереходів і забезпечують надійну основу для оптимізації кріогенних оптоелектронних, наноелектронних та високопольових напівпровідникових пристроїв.

Ключові слова: *гетеропереходи Si/GaAs; розподіл електричного поля; неповна іонізація домішок; кріогенні температури; область збіднення*